Troy+ brain stem cells cycle through quiescence and regulate their number by sensing niche occupancy

Onur Basak[a,b,1], Teresa G. Krieger[c], Mauro J. Muraro[a,b], Kay Wiebrands[a,b], Daniel E. Stange[a,b,2], Javier Frias-Aldeguer[a,d], Nicolas C. Rivron[a,d], Marc van de Wetering[a,b,e], Johan H. van Es[a,b], Alexander van Oudenaarden[a,b], Benjamin D. Simons[c,f,g,3], and Hans Clevers[a,b,e,3]

[a]Hubrecht Institute, Royal Netherlands Academy of Arts and Sciences and University Medical Center Utrecht, 3584 CT, Utrecht, The Netherlands; [b]Cancer Genomics Netherlands, University Medical Center Utrecht, 3584 GC, Utrecht, The Netherlands; [c]The Wellcome Trust/Cancer Research UK Gurdon Institute, University of Cambridge, Cambridge CB2 1QN, United Kingdom; [d]MERLN Institute for Technology-Inspired Regenerative Medicine, Maastricht University, 6229ER, Maastricht, The Netherlands; [e]Princess Máxima Centre, 3584 CT, Utrecht, The Netherlands; [f]Cavendish Laboratory, Department of Physics, University of Cambridge, Cambridge CB3 0HE, United Kingdom; and [g]Wellcome Trust-Medical Research Council Stem Cell Institute, University of Cambridge, Cambridge CB2 1TN, United Kingdom

Contributed by Hans Clevers, November 7, 2017 (sent for review September 11, 2017; reviewed by Francois Guillemot and Ana Martin-Villalba)

The adult mouse subependymal zone provides a niche for mammalian neural stem cells (NSCs). However, the molecular signature, self-renewal potential, and fate behavior of NSCs remain poorly defined. Here we propose a model in which the fate of active NSCs is coupled to the total number of neighboring NSCs in a shared niche. Using knock-in reporter alleles and single-cell RNA sequencing, we show that the Wnt target *Tnfrsf19*/Troy identifies both active and quiescent NSCs. Quantitative analysis of genetic lineage tracing of individual NSCs under homeostasis or in response to injury reveals rapid expansion of stem-cell number before some return to quiescence. This behavior is best explained by stochastic fate decisions, where stem-cell number within a shared niche fluctuates over time. Fate mapping proliferating cells using a Ki67^{iresCreER} allele confirms that active NSCs reversibly return to quiescence, achieving long-term self-renewal. Our findings suggest a niche-based mechanism for the regulation of NSC fate and number.

neural stem cells | cellular dynamics | modeling | single-cell sequencing | ki67

Adult stem cells often reside in niche structures composed of specialized cells. This creates a microenvironment in which specific signals maintain and regulate the resident stem-cell pool (1). The adult mouse subependymal zone (SEZ) of the lateral ventricles provides a model system to study the mammalian neurogenic niche (2–5). Extrinsic niche signals as well as intrinsic factors contribute to the maintenance of a pool of neural stem cells (NSCs) that generate neuroblasts (NBs) through rapidly dividing transit-amplifying (TA) cells. NBs migrate anteriorly along blood vessels and the rostral migratory stream to the olfactory bulb (OB), where they differentiate into several types of interneurons (6–8). In humans, NSCs also persist in adulthood and might contribute to striatal neurogenesis, raising hopes for their therapeutic potential. However, the functional significance of newly formed adult neurons remains unresolved (6).

Both FACS analysis and viral lineage tracing experiments provide strong evidence that a subset of SEZ astrocytes contacting the ventricles (B_1 cells) are NSCs (9). Visualization of the ventricular surface *en face* shows that ependymal cells, which cover the ventricular surface, surround the apical end feet of B_1 astrocytes (10). This characteristic spatial organization results in the formation of hallmark "pinwheel" structures (8, 9) (Fig. 1*A*). The apical end feet provide access to the cerebrospinal fluid, which is rich in extrinsic signals, and to axons that regulate neurogenic activity (11, 12).

Several characteristic pathways have been implicated in the regulation of adult NSCs. While ependymal cells have motile cilia, B_1 astrocytes have a single primary cilium that is involved in sonic-hedgehog signaling that regulates NSC identity (13, 14). Ependyma, astrocytes, active NSCs (aNSCs), and NBs present the Notch ligands Jagged1 and Dll1 that promote NSC self-renewal through Notch signaling (15–17). Both the Notch and PEDF signaling pathways are involved in maintaining NSC number (18–21). The bone morphogenic protein ligands as well as receptors are expressed by quiescent NSCs (qNSCs), which together with Notch, Wnt, insulin-like growth factor 2, VEGF, and EGF signaling pathways regulate quiescence, proliferation, and differentiation in the adult neurogenic niche (15, 18–25). In addition, basal processes of NSCs contact the blood vessels, which are thought to contribute to the regulation of stem-cell activity and might represent a route to relay systemic signals (5, 26, 27).

Retroviral labeling, BrdU label-retention experiments, and injury models that target proliferating cells all indicate that NSCs are predominantly out of the cell cycle (8). qNSCs are thought to enter into the cell cycle only rarely, generating aNSCs that contribute to adult neurogenesis before returning to quiescence

Significance

Adult mammalian tissues contain stem cells that contribute to tissue homeostasis and regeneration, with potential therapeutic applications. Specialized niches regulate their fate. Here we evaluated quantitatively how the subependymal zone niche regulates neural stem cell (NSC) number in the adult mouse brain. Using knock-in reporter alleles and single-cell RNA sequencing, we show that the Wnt target *Tnfrsf19*/Troy identifies both active and quiescent NSCs. Using the Ki67-iresCreER mouse model, we found that dividing stem cells have long-term self-renewal potential. We propose a model where the fate of NSCs is coupled to their density within a closed niche. Our results suggest a new mechanism for regulating adult stem cell number, which might be deregulated in brain malignancies and in aging.

Author contributions: O.B., T.G.K., B.D.S., and H.C. designed research; O.B., J.F.-A., M.v.d.W., and J.H.v.E. performed research; D.E.S. contributed new reagents/analytic tools; O.B., T.G.K., M.J.M., K.W., N.C.R., A.v.O., and B.D.S. analyzed data; and O.B., T.G.K., B.D.S., and H.C. wrote the paper.

Reviewers: F.G., The Francis Crick Institute; and A.M.-V., German Cancer Research Center.

The authors declare no conflict of interest.

Data deposition: The data reported in this paper have been deposited in the Gene Expression Omnibus (GEO) database, https://www.ncbi.nlm.nih.gov/geo (accession no. GSE65970).

[1]Present address: Department of Translational Neuroscience, Brain Center Rudolf Magnus, University Medical Center Utrecht and Utrecht University, 3584CG Utrecht, The Netherlands.

[2]Present address: Department of Visceral, Thoracic and Vascular Surgery, University Hospital Carl Gustav Carus, Technische Universität Dresden, 01069 Dresden, Germany.

[3]To whom correspondence may be addressed. Email: bds10@cam.ac.uk or h.clevers@hubrecht.eu.

This article contains supporting information online at www.pnas.org/lookup/suppl/doi:10.1073/pnas.1715911114/-/DCSupplemental.

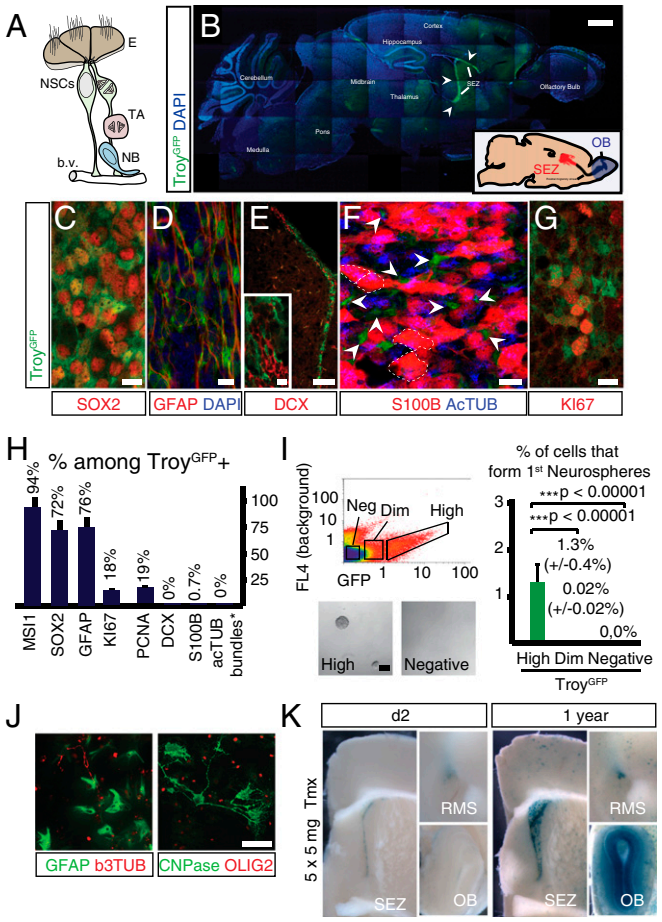

Fig. 1. Troy^{GFP} population displays NSC characteristics. (*A*) Schematic representation of the adult SEZ niche. b.v., blood vessels; E, ependymal cells; TA, transient amplifying cell. (*B*) Endogenous GFP (green) expression in the adult Troy^{GFP} mouse brain. Blue: DAPI. (*C–H*) Characterization of the Troy^{GFP} population using confocal assisted immunohistochemistry. Troy^{GFP} cells include SOX2+ (*C*) and GFAP+ (*D*) progenitors but not DCX+ NBs (*E*) or S100β+ E cells (*F*). Some Troy^{GFP} cells are actively cycling (KI67+, *G*). (*H*) Quantification of the results in *C–G*. (*I*) FACS-sorted GFP+ cells were assayed for their neurosphere-forming potential. (*J*) Individual Troy$^{GFP\text{-}high}$-derived spheres (40/40 spheres, five animals) could be expanded over at least 10 passages and displayed multipotency generating β3-tubulin+ neurons (red, *Left*), GFAP+ astrocytes (green, *Left*), and CNPase+ (red, *Right*) Olig2+ (green, *Right*) oligodendrocytes upon differentiation. (*K*) Lineage tracing using Troy^{GFPiresCreER} Rosa^{LacZ} mice. X-Gal staining of coronal sections of brains isolated 2 d (*Lower Left*) or 1 y (*Lower Right*) after 5 d of Tmx administration (1 × 5 mg each day). Error bars show SD. (Scale bars: *B*, 1 mm; *C* and *G*, 10 μm; *D* and *F*, 20 μm; *E*, 100 μm; *J*, 100 μm.)

or differentiating (8, 28–30). However, the fate behavior of individual NSCs remains undefined. In the "classical" model, maintenance of the NSC population is thought to involve serial rounds of invariant asymmetric cell division. In this paradigm, following entry of qNSCs into the cycle only one daughter cell returns to quiescence, while the other differentiates into a TA cell either directly or through a series of terminal divisions (31). Alternatively, the fate behavior of NSCs could be stochastic such that, upon activation, an average of one aNSC returns to quiescence for every qNSC that enters into the cell cycle. In the first paradigm, which we term "division asymmetry," only qNSCs maintain long-term self-renewal potential while, in the second, termed "population asymmetry," self-renewal potential is shared by quiescent and aNSCs and achieved only at the population level. Finally, another intriguing possibility is that the NSC pool is "disposable" so that, once activated, they either differentiate directly or stay in the cell cycle, becoming exhausted over time.

Recently, evidence in favor of the "disposable" stem cell model has been provided by genetic lineage tracing and live-imaging studies, which suggest that aNSCs eventually lose neurogenic potential (32–35). Studies based on the direct visualization of radial glia in slice cultures as well as invertebrate models have placed emphasis on invariant asymmetric cell division (36). However, evidence in support of either niche-directed asymmetric NSC division or the spontaneous segregation of fate determinants is currently lacking. Alongside their identity and fate behavior, the nature of NSC regulation also remains unresolved: In particular, does the fate behavior of NSCs follow from intrinsic (cell-autonomous) regulation or through interactions with the local environment? If the latter, do NSCs explore an open or facultative niche, or are they confined to a closed domain?

Here, we have combined long-term genetic lineage tracing assays and detailed quantitative analysis of clone fate with single-cell RNA expression profiling to resolve the molecular identity, functional heterogeneity, self-renewal potential, and fate behavior of NSCs in the SEZ of adult mice.

Results

Troy Marks Adult NSCs in the SEZ. The Wnt signaling pathway is pivotal for the maintenance of multiple adult stem-cell populations (37). However, its role in regulating SEZ NSC fate is poorly understood (38–40). Recently, the Wnt target *Tnfrsf19*/Troy has been found to mark active intestinal stem cells and a quiescent stem-cell population in the stomach (41, 42). Since Troy expression has been reported in the SEZ (43), we questioned whether Troy+ cells may be NSCs and used the Troy$^{GFPiresCreER\ +/HET}$ knock-in mouse to characterize their functional behavior in adult neurogenesis.

We found Troy^{GFP} expression (visualized by endogenous fluorescence) to be highly restricted to the SEZ (Fig. 1*B* and *SI Theory*). Analyzed by immunohistochemistry, Troy^{GFP}+ cells expressed progenitor markers MSI1 and SOX2 (94 ± 9% and 72 ± 11% of Troy^{GFP} + cells, respectively) as well as the astrocyte/stem-cell marker GFAP (76 ± 9%; Fig. 1 *C*, *D*, and *H* and Fig. S1 *A* and *B*), but did not express the NB marker doublecortin (DCX; 0 ± 0%; Fig. 1 *E* and *H*); 0.7 ± 0.7% of Troy^{GFP}+ cells expressed the astrocyte/ependymal marker S100β (Fig. 1 *F* and *H*). These Troy^{GFP}+S100β+ cells were located below the ventricular surface and showed astrocyte-like processes (Fig. S1*C*). Consistently, acetylated tubulin staining confirmed that Troy^{GFP} + cells lacked ependymal-specific multiple motile cilia (Fig. 1 *F* and *H*). Of note, we could not detect endogenous Troy^{GFP} expression in parenchymal astrocytes (Fig. 1 *B* and *D*). While some Troy^{GFP}+ cells were observed to be in the cell cycle, as indicated by proliferating cell nuclear antigen (PCNA; 19 ± 2%) and KI67 (18 ± 2%) expression, they formed only a fraction of proliferating SEZ cells (24 ± 10% of KI67+ cells; Fig. 1 *G* and *H* and Fig. S1*D*); 72 ± 30% of the GFAP+ SEZ astrocytes expressed Troy^{GFP}, while none of the S100β+ ependyma with acetylated tubulin bundles (0 ± 0%) and DCX+ NBs (0 ± 0%) expressed Troy^{GFP} (Fig. 1 *D–F* and Fig. S1*F*). Troy^{GFP}+ cells touched the ventricles between S100β+ ependyma and contacted blood vessels, both key morphological features of NSCs (Fig. 1*F* and Fig. S1*E*). Single-molecule FISH (smFISH) revealed that the average copy number of Troy mRNA per cell was highest in subependymal cells and low in cells lining the ventricles (Fig. S1*G*). While ependymal cells might express low levels of Troy mRNA, all Troy-high cells were subependymal. Some cells with low levels of Troy^{GFP} fluorescence were also visible in the blood vessels and in the parenchyma (Fig. 1*B*). These cells were never GFP-high and were outside the neurogenic niche and, as such, were not

analyzed further. The Troy^{GFP} population therefore includes both astrocytic and proliferating cells of the SEZ.

To investigate whether Troy+ cells could self-renew and differentiate into the diverse cell types of the adult brain we performed neurosphere assays. When placed in culture, we found that Troy$^{GFP\text{-}high}$ cells formed neurospheres (1.3 ± 0.4%) much more efficiently than Troy$^{GFP\text{-}low}$ and Troy$^{GFP\text{-}negative}$ cells (0.02 ± 0.02% and 0%, respectively; $P < 0.0001$; Fig. 1*I*). Individual Troy$^{GFP\text{-}high}$ cells displayed multipotency, differentiating into neurons, astrocytes, and oligodendrocytes (Fig. 1*J*). When compared directly to published NSC markers (15, 44), Troy$^{GFP\text{-}high}$ cells (1.8 ± 0.2%) generated neurospheres more efficiently than SLC1A3+EGFR− qNSCs (0 ± 0%; $P < 0.005$) and SLC1A3+PROM1− astrocytes (0.56 ± 0.12%; $P < 0.005$; Fig. S1*H*). SLC1A3+EGFR+ aNSCs and Troy$^{GFP\text{-}high}$ cells formed comparable numbers of neurospheres (2.23 ± 0.15%; $P = 0.048$; Fig. S1*H*). Thus, Troy^{GFP} cells display self-renewal potential and multipotency in vitro.

To probe the self-renewal and differentiation potential of Troy+ cells in vivo we used Troy$^{GFPiresCreER\ +/HET}$ Rosa$^{LacZ\ +/HET}$ mice where tamoxifen (Tmx) injection results in heritable activation of LacZ expression (Fig. 1*K*). Following five rounds of daily Tmx injection, labeled cells were confined to the SEZ at 2 d postinduction and robustly populated the OB over time (Fig. 1*K*). Recombined cells remained in the SEZ even after 6 mo and 1 y postlabeling and generated new NBs, identifying Troy as a marker whose expression pattern overlaps with that of the adult NSC pool (Fig. 1*K* and Fig. S1 *I*–*S*).

Single-Cell Whole Transcriptome Atlas of Adult Neurogenesis. To characterize the molecular features and heterogeneity of Troy+ NSCs we generated a single-cell atlas of adult neurogenesis in the SEZ using Sort-seq, which combines FACS with automated single-cell RNA sequencing (45, 46) (Fig. 2*A* and Fig. S2*A*; see *SI Theory* for further details on this section). We isolated cells using key published surface markers (15, 47), Slc1a3 (NSCs), and EGF binding ability (dividing cells), as well as reporters based on transgenic mouse models Troy^{GFPiresCreER} (NSCs) and Ki67^{RFP} (dividing cells) (48), among others. We then used the RaceID2 algorithm to cluster 1,465 cells which passed our quality control, based on similarity of their transcriptome to find virtually all cell types present in the SEZ (Fig. S2*A* and Dataset S1). Focusing on the 1,205 cells that are on the NSC-to-neuron differentiation axis, we identified nine clusters showing a near-continuous variation in the pattern of expression together with a small isolated cluster on the t-distributed stochastic neighbor-embedding (t-SNE) map (Fig. 2 *A* and *B* and Fig. S2 *A* and *B*). We considered genes significantly enriched (false discovery rate <0.01) in a given cluster(s) compared with the rest of the dataset as their "molecular signature," as described before (49). These included Slc1a3/Hes5/Nr2e1+ NSCs (clusters 1, 2, 3, 4, and 6) where Troy^{GFP} sorted cells as well as Troy mRNA were enriched (15, 50, 51) (Fig. 2 *A* and *C* and Fig. S2*A*). Expression of Egfr and

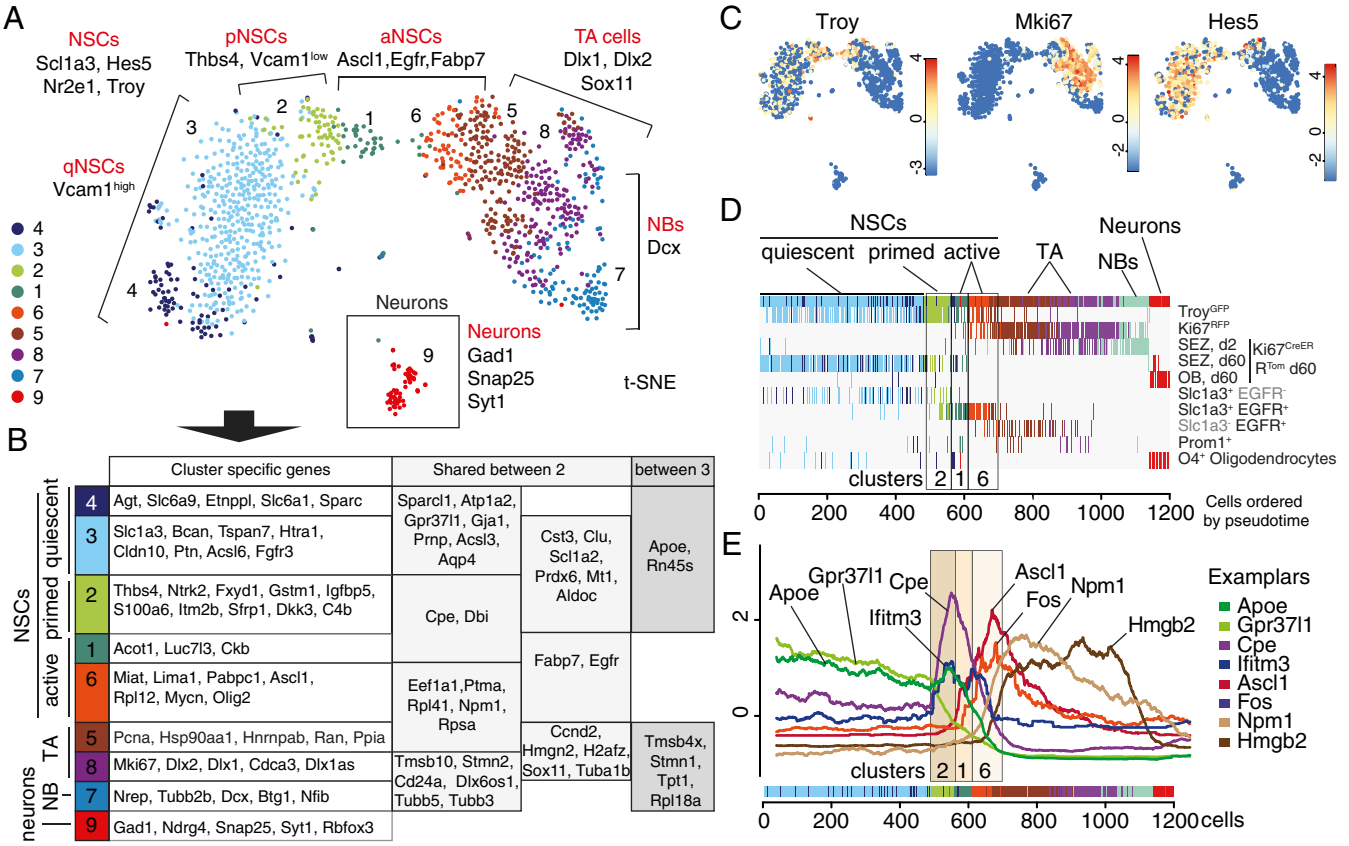

Fig. 2. Single-cell transcriptome atlas of adult neurogenesis. (*A*) A t-SNE map showing clusters identified by RaceID2 and expression of key marker genes. (*B*) Summary of genes differentially expressed in each cluster. Unique (left lane) as well as shared (middle and right lane) genes are shown. See Dataset S2 for a complete list. (*C*) t-SNE maps displaying the normalized log2 expression of key genes. The color key shows expression values. (*D*) Distribution of sorted cell populations along pseudotime. Putative cell types are indicated above. Boxes highlight clusters 2, 1, and 6. Colors code for RaceID2 clusters shown in *A*. (*E*) Plot displaying the running mean average expression levels of representative (exemplar) genes for selected gene modules. In *D* and *E*, cells are ordered on the *x* axis according to pseudotime; the color bar displays RaceID2 clusters.

Fabp7 identified aNSC clusters 1 and 6, the latter of which is enriched in Ascl1 (52) (Fig. 2 *A* and *B* and Fig. S2*C*). Marker expression identified Dlx1/Dlx2/Sox11+ clusters 5 and 8 as TA cells, Dcx+ cluster 7 as NBs, and Gad1, Snap25, and Rbfox3 cluster 9 (consistent with them being isolated from the OB) as neurons (Fig. 2*B* and Fig. S2 *A*–*D*). When placed in a linear order on the NSC–neuronal differentiation axis (pseudotime; see *SI Theory*). Troy^{GFP}+ NSCs were placed early and partially overlapped with Ki67^{RFP}+ and SLC1A3+EGFR+ (putative aNSCs) cells (53) (Fig. 2*D*). SLC1A3+EGFR− cells, with an expression profile similar to published signatures of qNSCs, also expressed Troy mRNA (Fig. S3*C*). Analysis of the single-cell transcriptome data provided independent evidence that Troy+ cells display key molecular features of NSCs and overlap with published stem cell signatures. A detailed analysis of the expression pattern of new and published markers is described in *SI Theory*. Here, we focused on the putative aNSCs to investigate the molecular basis of their functional differences.

For this purpose, we used coexpression of a selected set of genes as a proxy to define coregulated gene modules using the APCluster package (54) for affinity propagation clustering and identified 19 gene modules (Fig. 2*E*, Fig. S3 *E* and *F*, and Datasets S3 and S4). Most modules displayed marked changes in gene expression at intermediate points along the pseudotime axis, where cells of clusters 2, 1, 6, and 5 reside (Fig. 2*E* and Fig. S3*F*). In contrast, cell cycle-related gene modules were up-regulated almost simultaneously along the pseudotime axis from cluster 6 onward, demonstrating that dividing and nondividing cell types were clearly separated (Fig. S3*G*). Consistently, ribosomal gene expression displayed a three-stage pattern: low in clusters 4 and 3 (qNSCs), medium in clusters 2 (NSCs primed for activation, pNSCs) and 1 (aNSCs), and high in clusters where cell cycle-related gene expression is elevated (Fig. S2*C*).

Apart from cell cycle-related modules, changes in gene expression do not occur simultaneously, which argues against a single molecular switch of differentiation (Fig. 2*E*). Instead, Gpr37l1, Apoe, and Slc1a2 modules all diminish at different points along the pseudotime axis (Fig. 2*E*). An initial peak of expression of the carboxypeptidase E (Cpe) gene module in primed NSCs was followed by peaks of Ascl1 and Fos gene modules in aNSCs. Expression of Npm1, Hmgb2, Hnrnpab, and Sox11 modules initiated at distinct points in aNSCs along the pseudotime axis and persisted in putative TA cells (Dlx2+) and NBs (Dcx+) (Fig. 2*E* and Fig. S3*F*). Similarly, signaling pathway components and surface receptors implicated in cell fate decisions display a complex pattern in aNSCs (Fig. S3*H*). This behavior is consistent with the absence of a "point of no return," where the distinction between traditional NSCs and TA cells is clear-cut.

In summary, these findings suggest that niche-related signaling pathways display dynamic changes along the NSC–neuronal differentiation axis and distinct expression in aNSCs, which may continuously adjust their differentiation potential.

Troy+ NSCs Undergo Limited Proliferation Within Clones. Recent studies have suggested that individual aNSCs do not retain long-term self-renewal potential but become exhausted within a few weeks of activation (33). Thus, ongoing neurogenesis would require constant activation of additional qNSCs over time. To resolve the dynamics of NSC activation, division, and maintenance we employed a genetic lineage tracing approach to trace the progeny of individual marked Troy+ cells over time. A single injection of Tmx (50 mg/kg) in Troy$^{GFPiresCreER\ +/HET}$ Rosa$^{YFP\ +/HET}$ mice generated ~85 clones per cerebral hemisphere, which we analyzed by position and cell composition at 2 and 4 d as well as 1, 2, 4, 8, 16, and 32 wk postrecombination (Fig. 3 *A* and *B* and *Methods*). The entire neurogenic niche was visualized *en face* by generating a 3D reconstruction from confocal images (55). We confirmed that Troy^{GFP} signal does not leak into the and Rosa^{YFP} channel, allowing independent detection of the channels (Fig. S4*A* and *SI Theory*). One week after recombination,

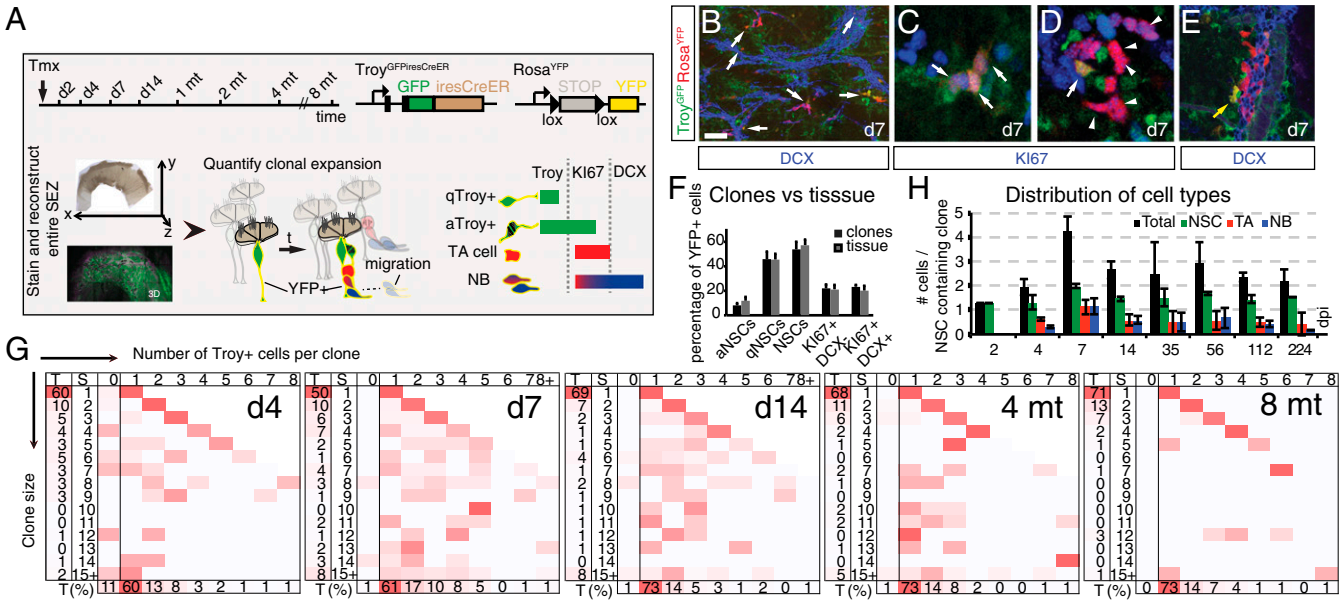

Fig. 3. Analyzing the Troy+ lineage at a clonal level. (*A*) Schematic representation of the lineage-tracing experiment. (*B*–*E*) Representative clones identified as clusters of YFP+ cells (*B*); migratory NBs were excluded from the analysis. One week after Tmx induction, clones with multiple dividing Troy^{GFP}+ cells (*C*), both dividing Troy^{GFP}+ cells and differentiating progeny (*D*), as well as large with a quiescent Troy^{GFP}+ cell and differentiating progeny (*E*) were visible within the same sample. (*F*) Comparison of the composition of clones at d 7 to the tissue. (*G*) Quantification of the number of Troy^{GFP}+ cells with respect to the clone size over time. Percentages (T, total) on the left and at the bottom show aggregated numbers. S, size. (*H*) Average composition of different cell types in clones that retain NSCs scored over time. (Scale bar: 60 μm for *B*, 5 μm for *C* and *D*, and 20 μm for *E*.)

some of the recombined YFP+ cells coexpressed Troy^{GFP} and the astrocyte marker GFAP and displayed astrocytic morphology (Fig. S4*B*). Recombined cells did not express S100β (0 ± 0%) and were not multiciliated (0 ± 0%), indicating that the ependyma is not labeled with our induction regimen (Fig. S4 *C* and *D*). After 1 mo, labeled YFP+ cells migrated to the granule and periglomerular layers of the OB to generate new neurons, including NeuN+ or Calretinin+ subtypes (Fig. S4*E*). Using KI67 as a pan-proliferation marker and DCX as a neuronal differentiation marker, we classified cells within clones as qNSCs (Troy^{GFP}+KI67−) or aNSCs (Troy^{GFP}+KI67+), TA cells (Troy^{GFP}−KI67+DCX−), or early NBs (Troy^{GFP}−KI67+DCX+) (Fig. 3 *B*–*E*). Since postmitotic NBs (KI67−DCX+) rapidly migrate away from their source, we excluded them from our analysis (Fig. 3 *A* and *B*). We confirmed by nearest-neighbor distance analysis that mergers between clones were highly unlikely (*SI Theory* and Fig. S4*F*). No correlation was observed between the location of a clone in the SEZ and its size or composition, suggesting that clonal behavior is independent of the spatial position of NSCs (Fig. S4*G*). Further, the cellular composition of clones by 7 d postinduction mirrored that of the surrounding tissue, implying that Troy^{GFP} expression marks a representative population of NSCs (Fig. 3*F*).

Throughout the time course most clones were composed of a single qNSC (Fig. S4*H*). Small clones with at least one cycling cell (fewer than five cells) consisted almost entirely of aNSCs (Fig. 3*C*, arrows, Fig. 3*G*, and Fig. S4*H*). For larger clone sizes, a decline in the number of aNSCs was accompanied by an increase in TA cell number (Fig. 3*D*, arrowheads, Fig. 3*G*, and Fig. S5*A*). The largest clones typically contained several NBs and a single qNSC (Fig. 3*E*, yellow arrow). However, aNSCs persisted in clones even at 8 mo postinduction, consistent with the continuous production of olfactory neurons from Troy+ cells (Fig. 3*G* and Fig. S4 *H* and *I*).

Previous studies have proposed that NSCs undergo invariant asymmetric cell division in which only one of the daughter cells retains stem-cell competence (56, 57). In contrast, we found that clones at early time points were composed primarily of multiple Troy^{GFP}+ cells, suggesting that NSCs are capable of symmetric division upon activation (Fig. 3*C* and Fig. S4*H*). Further, the size and composition of Troy-traced clones did not change significantly from day 14 onward, with each clone containing 1.5 ± 0.1 Troy^{GFP}+ cells on average (Fig. 3*H*). This shows that NSC proliferation is thus balanced by differentiation and loss through cell migration.

Such clonal behavior resonates with lineage tracing studies of other adult tissues where homeostasis follows from population asymmetry, with stochastic stem cell differentiation and loss compensated by the duplication of neighboring stem cells (58). However, within such a framework the number of stem cells in individual clones would then be predicted to evolve according to "neutral drift" dynamics in which some clones undergo chance expansion while others would contract or become lost through differentiation so that the total number of NSCs remains constant over time. As a result, the number of surviving clones would gradually decrease over time while the average number of NSCs per surviving clone would gradually increase. Here, in contrast, both the density of NSC-retaining clones and their stem-cell content (as indicated by the average number of Troy^{GFP}+ cells per clone) remained constant from day 14 onward (Fig. 4 *A* and *B*). Stem cells in the SEZ thus do not conform to a simple pattern of neutral drift dynamics as observed in adult epithelial tissues.

To determine how the Troy+ stem-cell pool is maintained in the SEZ we focused on the actively cycling and quiescent stem-cell content of clones. We found that, at any given time postinduction, a fraction of clones contained only aNSCs (Fig. S5*B*). Since the density of clones in the SEZ remained approximately

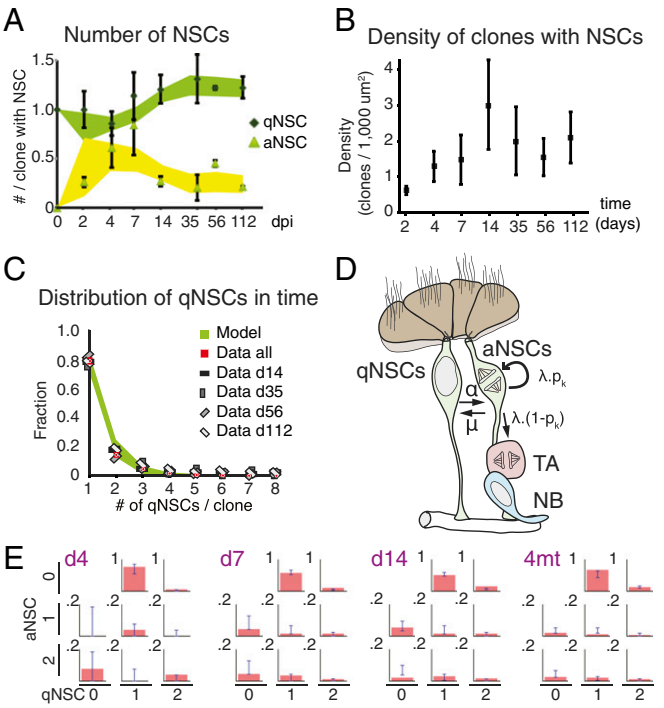

Fig. 4. A restricted niche regulates adult NSC numbers. (*A*) Average number of active (aNSC) and quiescent (qNSC) NSCs per NSC-containing clone scored over time alongside model predictions (shaded areas indicate 95% plausible intervals). (*B*) Density of NSC-retaining clones over time. (*C*) Distribution of the number of qNSCs per NSC-containing clone averaged over time points between d 14–112 and model prediction (95% plausible intervals). (*D*) Schematic representation of the model of niche regulation of NSC numbers. qNSCs become activated at rate α, while aNSCs return to quiescence at rate μ or divide at rate λ. When an aNSC divides in a niche containing a total of k NSCs (active or quiescent), it undergoes symmetric cell duplication with a probability p_k and symmetric differentiation with a probability $1-p_k$, with $p_k = 1/k^x$ and $x = 0.9 \pm 0.1$ (see *SI Theory* for details). (*E*) Sample plots comparing the fraction of clones with given aNSC and qNSC composition estimated by simulation of the model (bars) to collected data (red bars) at various time points.

constant over time (Fig. 4*B*), it follows that these clones are not lost from the tissue. This implies that aNSCs must be able to return to long-term quiescence after one or more rounds of cell division. Further, the average qNSC and aNSC content of clones also remained constant from day 14 onward, indicating that, on average, one aNSC must return to quiescence for every qNSC that becomes activated (Fig. 4*A*).

If the pattern of self-renewal and the return of aNSCs to quiescence were stochastic processes, regulated by cell-autonomous factors, then one would expect to find some clones at later time points containing an increasing number of qNSCs. Instead, the frequency of clones with a given number of qNSCs remained constant from day 14 onward (i.e., while the size and composition of individual clones may fluctuate over time, when averaged across the ensemble, the distribution becomes stationary) (Fig. 4*C*). Within this distribution, most clones (78 ± 2%) contain just one qNSC while others contain as many as seven. As clones are not lost from the SEZ over time, the self-renewal probability of an NSC dividing in a niche containing no other stem cells is unity (since otherwise clones would not be maintained long-term). In order for the distribution of NSCs in clones to remain constant from 14 d postlabeling, it then follows that when an NSC divides in a niche containing more than one stem cell its self-renewal probability decreases with the number of NSCs already present in the local niche (otherwise the average number of NSCs within

clones would grow over time, and their distribution would grow broader). Crucially, the convergence of clone sizes onto a stationary distribution thus shows that aNSC fate is not determined by a cell-intrinsic mechanism, since persisting clones do not continue to expand in size over time. Instead, it must follow from a cell-extrinsic mechanism, where aNSC fate is conditioned by the behavior of neighboring stem cells.

Taken together, these results suggest that the SEZ is organized into a 2D array of isolated niche domains that each host a variable but limited number of qNSCs and aNSCs. Following pulse labeling of NSCs using the Troy promoter, a short period of clonal competition becomes resolved in the clonal "fixation" of qNSCs and aNSCs within the niche, after which the average clone density and size distribution become constant. In this model, at long chase times, variability of individual clone sizes reflects a continuous and dynamic process of NSC activation, expansion, contraction, and deactivation that, when averaged across the ensemble of clones, leads to the observed stationary size distribution.

Troy+ NSC Dynamics Are Consistent with a Restricted Niche Model. To determine whether such a restricted niche-based mechanism could result in the observed dynamics we developed a simple and predictive model of NSC behavior in the SEZ (Fig. 4*D* and *SI Theory*). Within this model, qNSCs become activated sporadically at a constant rate and enter into cycle, while aNSCs stochastically return to quiescence at another constant rate. During their active phase, NSCs may independently and stochastically choose between cell duplication, giving rise to two aNSCs, and a symmetric differentiating division generating two TA cells. For simplicity, we do not consider explicitly asymmetric fate outcome since such events can be captured within the model as a combination of the two symmetrical fates (*SI Theory*). The stationarity of the clone size distribution at longer chase times indicates that NSC number within clones must be locally constrained. To accommodate this observation, we proposed that individual aNSC divisions result in cell duplication or symmetric differentiation with a relative probability that depends on the total number of existing NSCs (active or quiescent) in the local neighborhood or niche (Fig. 4*D*). Further, to ensure the observed long-term survival of clones, we imposed the condition that a single NSC occupying a niche always divides symmetrically, giving rise to two NSCs. As the number of neighboring NSCs in the niche increases, the fate of aNSCs becomes gradually more biased toward differentiation into TA cells, effectively restricting the capacity of the niche. Over time, these "rules" translate to dynamics in which, on average, one NSC returns to quiescence for each NSC that becomes activated. Therefore, while the NSC and TA cell content of individual clones fluctuates over time (Fig. 3*H*), once the niche becomes clonally fixed the average total number of NSCs, the average number of aNSCs, and the corresponding clone size distributions are all maintained constant over time, as observed (Figs. 3*H* and 4*A* and Fig. S4 *H* and *I*).

To infer the rates of NSC activation, division, and return to quiescence we adopted a maximum-likelihood approach (*SI Theory*). Scanning the space of possible parameters, we performed stochastic simulations to determine for every parameter combination the expected clone size distributions based on the proposed NSC dynamics. By comparing these predictions with the experimentally observed clone size distributions we deduced the "best-fit" parameters. These corresponded to a qNSC activation rate of once per 20 ± 4 d, an aNSC division rate of once per 16 ± 2 h, and a rate of return to quiescence of once per 5 ± 2 d. With these parameters we found that the model could recapitulate the full joint distribution of qNSCs and aNSCs in clones, from the transient short-term dynamics, up to 14 d postlabeling, to the longer-term steady-state behavior (Fig. 4 *D* and *E*, *SI Theory*, and Fig. S5 *C–E*).

Once activated, the model predicts that NSCs go through an average of ∼2.7 rounds of division before they return to quiescence or differentiate, giving rise to ∼3.4 TA cells that proceed to generate neurons (Fig. 4*D*, *SI Theory*, and Fig. S5*F*). Note that the inclusion of additional contributions from aNSC divisions leading to asymmetric fate outcome may revise these estimates. However, our inferred aNSC division rate is consistent with existing estimates from the literature (57). Moreover, few clones in our data contain both aNSCs and differentiating progeny (Fig. S5*A*). If asymmetric aNSC divisions occur at all, their relative frequency is therefore likely to be small. To develop the model of NSC behavior above we relied on measures of the functional behavior of Troy+ NSCs. To test the representativeness of Troy labeling, and the quantitative predictions of the model, we turned to an independent and unbiased labeling strategy.

Fate Mapping of Proliferating Cells Confirms Expansion of NSCs Within the Niche. Our model, which is based on population asymmetric self-renewal, suggests that actively cycling NSCs are not committed to differentiation but may return to quiescence. To challenge our model with an independent approach, we generated a second in vivo genetic labeling system to trace the fate of proliferating cells, including aNSCs (see *SI Theory* for further details on this section). Specifically, we used KI67 expression as a proxy for cells in the G_1, S, G_2, and M phases of the cell cycle, as opposed to quiescent cells resting in the G_0 state (59). We generated the $Ki67^{iresCreER}$ mouse by inserting an $iresCreER^{T2}$ coding sequence downstream of the stop codon in the last exon of the *Mki67* gene (Fig. S6*A*). Recombination in $Ki67^{iresCreER\ +/HET}$ $Rosa^{tdTomato\ +/HET}$ mice resulted in labeling (tdTomato expression) of both KI67+ dividing cells (51 ± 5% of tdTomato+ cells) and their immediate nondividing DCX+ progeny 1 d postrecombination (47 ± 3% of tdTomato+ cells, Fig. 5 *A–C*). To test the specificity of the $Ki67^{iresCreER}$ allele, we sequenced single tdTomato+ cells 2 d after recombination. Most tdTomato+ cells expressed multiple (and each cell expressed at least one of the) well-known cell cycle genes, indicating that the $Ki67^{iresCreER}$ allele labels cycling cells (Fig. S3*D*). A single BrdU injection 1 d before Tmx induction (d 0) labeled 35 ± 15% of the tdTomato+ KI67− cells at day 2 (Fig. S6 *B* and *C*), indicating that some of the cycling $Ki67^{iresCreER}$ labeled cells exit the cell cycle during this period. tdTomato+ cells continued to contribute to adult neurogenesis 1 y postrecombination, indicating that not only TA cells but also aNSCs are targeted by the $Ki67^{iresCreER}$ allele (Fig. 5 *B* and *C* and Fig. S6 *D–F*). In summary, these results show that the $Ki67^{iresCreER}$ mouse allele allows fate mapping of dividing cells in the adult SEZ.

To identify NSCs we focused on the tdTomato+ cells that contact the ventricles in the pinwheel niche structures (Fig. 5*D*). Consistent with the Troy data, most pinwheels contained just a single tdTomato+ NSC at all time points (Fig. 5*E*). While most NSCs were active (80 ± 5%) at 1 d postinduction, all single NSCs were KI67− by 1 wk, 1 mo, and 1 y postinduction, confirming that aNSCs can return to long-term quiescence (Fig. 5 *D* and *E*). Moreover, some pinwheels contained multiple qNSCs at 1 wk, 1 mo, and 1 y postinduction (13 ±13% of all pinwheels), indicating clonal expansion (Fig. 5 *E* and *F*). At 2 mo postinduction, progeny of marked Ki67+ cells colocalized with NSCs and expressed Troy mRNA, consistent with dividing aNSCs' having the capacity to generate Troy+ qNSCs (Fig. 2*D* and Fig. S3*C*). Thus, the Ki67 lineage tracing data confirmed that, while the majority of aNSCs exit cell cycle within a short period of time, some aNSCs expand within their niche before returning to quiescence. Moreover, the qNSC progeny of aNSCs may persist long-term, reenter the cell cycle, and contribute to ongoing adult

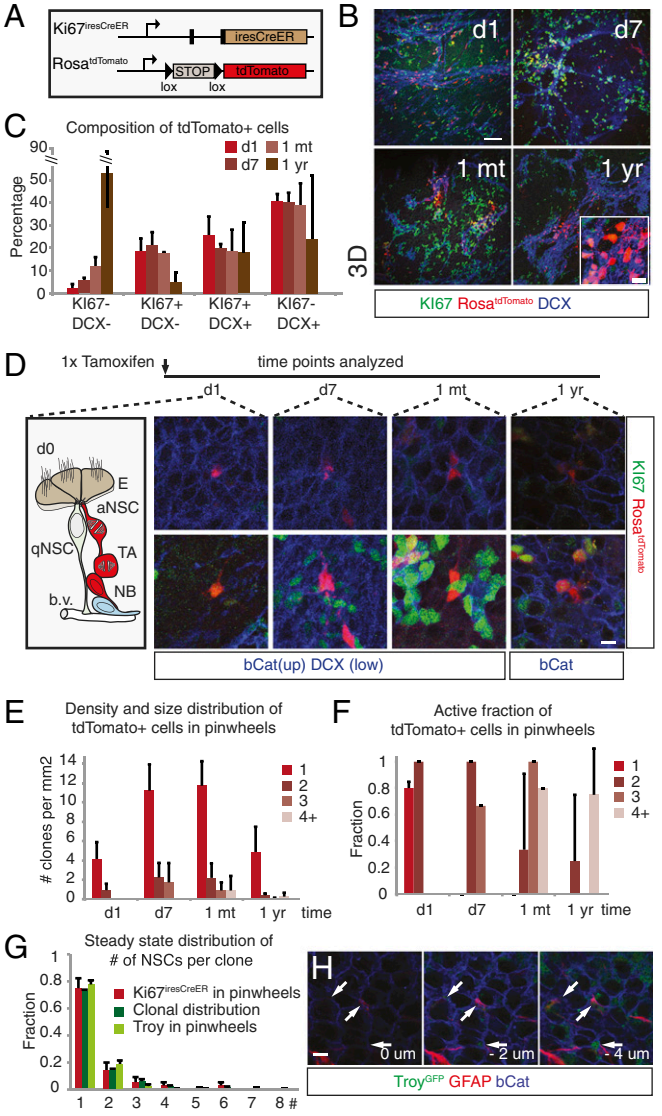

Fig. 5. aNSCs return to long-term, reversible quiescence. (*A*) Mouse alleles used for lineage tracing. (*B*) Characterization of the KI67^{iresCreER} Rosa^{tdTomato} lineage tracing d 1, d 7, 1 mo, and 1 y after a single injection of 250 mg/kg Tmx. (*C*) Quantification of cell types shown in *B*. (*D*) As depicted (schematic), tracing starts from aNSCs, TA cells, and some NBs. Contact to the ventricular surface is visualized by β-catenin (at the surface). Differentiation status is evaluated using KI67 and DCX (4 μm below the surface). (*E*) Density (number of clones per mm^2) and size distribution of tdTomato+ clones contacting the ventricles. (*F*) Quantification of *D* displaying active fraction (KI67+/tdTomato+) of tdTomato+ cells in pinwheels of a given size. (*G*) Comparison of the frequency of tdTomato+ cells per pinwheel in KI67$^{iresCreER\ +/HET}$ Rosa$^{tdTomato\ +/HET}$ mice (red) with the steady-state distribution (d 14 onward) of Troy^{GFP}+ cells in clones (clonal distribution, dark green) and the number of Troy^{GFP}+ cells per pinwheel (light green) in Troy$^{GFPiresCreER\ +/HET}$ Rosa$^{YFP\ +/HET}$ mice. (*H*) Optical sections showing contact of Troy^{GFP}+ (green) GFAP+ (red) NSCs to the ventricular surface. (Scale bars in *B*, *D*, and *H*, 10 μm.)

neurogenesis. By transiting reversibly between active and quiescent states, NSCs are able to achieve long-term self-renewal. These results are consistent with our model predictions and provide an independent confirmation of the heterogeneity of cellular dynamics within the NSC compartment.

The sensitivity of aNSC fate to the total number of NSCs within the same clone suggests that NSCs can sense and "count" the number of neighboring stem cells within their local niche. Pinwheel structures in the SEZ provide a candidate anatomical feature that demarcates separate niche domains (9). The Troy^{GFP} population includes cells in the pinwheels (B_1 cells) as well as cells placed deeper in the SEZ (B_2 cells). Consistent with this hypothesis, we found that the distribution of Troy^{GFP}+YFP+ cell numbers in putative pinwheel structures was strikingly similar to the observed steady-state distribution of all Troy^{GFP}+ cells in clones (Fig. 5 *G* and *H*). Moreover, comparison of the distribution of tdTomato+ NSCs within pinwheels with the distribution of Troy^{GFP}+ NSCs within pinwheels, and with the steady-state distribution of NSCs in clones, showed that the distributions were also strikingly similar (Fig. 5 *G* and *H*). It was also consistent with the reported distribution of astrocytes in pinwheels, from which we could deduce that around one in three astrocytes in pinwheels is Troy^{GFP}+ (9) (*SI Theory* and Fig. S5*G*).

Dynamics of Troy+ qNSC Activation Following Niche Perturbation. To challenge the niche organization and proliferative potential of NSCs we perturbed the neurogenic niche. Previous studies have shown that qNSCs become activated upon injury and can regenerate the SEZ (3, 15). To study the response of NSCs to injury, we made use of 5-fluorouracil (5-FU) treatment, which is reported to deplete most proliferative cells in the SEZ (60). Through optimization we found that the majority of proliferative cells in the SEZ could be eliminated using a single i.p. injection of 250 mg/kg of 5-FU (*Methods* and Fig. S7*A*). To study the targeted response of NSCs on injury, we combined 5-FU injection with our clonal induction protocol using the Troy$^{GFPiresCreER\ +/HET}$ Rosa$^{YFP\ +/HET}$ mice (Fig. 6*A*; also see *SI Theory* for further details on this section).

Following Tmx administration, analysis of tissue 2 d after 5-FU injection revealed the large-scale depletion of KI67+ cells while Troy^{GFP}+ cells survived (Fig. 6*A* and Fig. S7*A*). Proliferation was visible all over the SEZ at 7 d after 5-FU treatment, consistent with published protocols (60). At this point, almost all (99 ± 1%) recombined cells were found to be Troy^{GFP}+ (Fig. S7*B*). More than half (52 ± 5%) of these cells were also KI67+ (Fig. 6 *A* and *B*), suggesting increased activation of qNSCs upon injury. Under homeostatic conditions most clones were composed of a single qNSC (Fig. S4*H*); 19 ± 4% of all clones surviving 5-FU treatment were composed of a single KI67+ Troy^{GFP}+ cell (Fig. 6*C* and Fig. S7*B*). Consistent with our observation that NSCs can increase their number upon activation, some 48 ± 4% of clones contained only aNSCs (Fig. 6 *B* and *C* and Fig. S7*C*). The increase in the fraction of clones that include aNSCs indicates recruitment of qNSCs into the cell cycle in response to injury, a feature of deep qNSCs (15).

However, by day 14 after 5-FU treatment significantly fewer clones were composed of a single aNSC (1 ± 2%; $P = 0.012$) or only aNSCs (5 ± 3%; $P < 0.001$) (Fig. 6*D* and Fig. S7 *C* and *D*). Rather, most recombined clones contained Troy^{GFP}–KI67+ DCX– TA cells and DCX+ NBs, confirming the restoration of neurogenesis from labeled, initially quiescent, Troy^{GFP}+ cells (Fig. 6*D* and Fig. S7*B*). Significantly, at this time point the distribution of NSC number within clones matched closely that found at day 14 postinduction under homeostatic conditions (Fig. 6*E*), suggesting that the integrity of the restricted niche domain remains intact even during regeneration. However, although the average number of NSCs per clone was set at around 1.5 ± 0.1 cells, consistent with the capacity of the unperturbed niche, the relative fraction of quiescent and aNSCs was tilted toward the latter, suggesting that NSC activity may subside only slowly during regeneration.

Next, we used the 5-FU–mediated killing of dividing cells to test the cell-cycle dynamics of Ki67^{iresCreER}-labeled cells. Injection of 5-FU (d 0) in Ki67^{iresCreER} Rosa^{tdTomato} mice abolished proliferation at d 2, quantified by the density of KI67+ cells (62.8 ± 8.2 compared with 2,012 ± 378 cells per mm^2 in controls; Fig. 6 *F* and *G*). Tmx treatment 1 d after (d 1) 5-FU treatment (d 0) led to

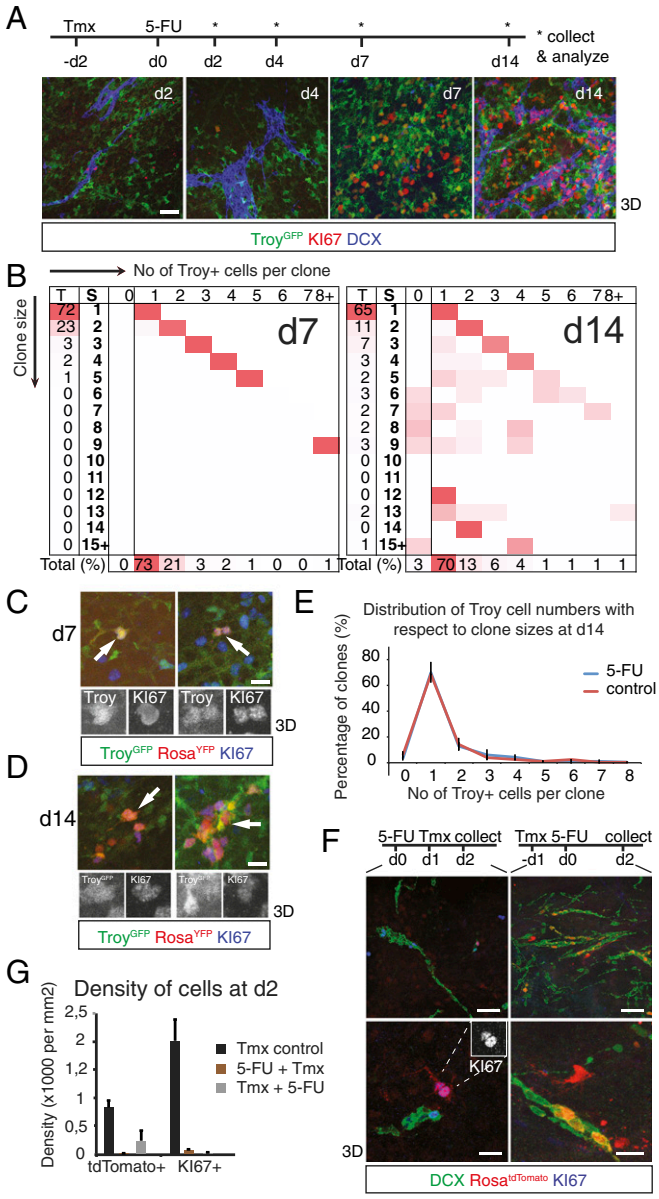

Fig. 6. Clonal dynamics of deep quiescent Troy+ NSCs activated during regeneration. (*A*) Injection of 5-FU abolishes proliferating cells in the SEZ. Recombination in Troy$^{GFPiresCreER\ +/HET}$ Rosa$^{YFP\ +/HET}$ mice was induced with Tmx 2 d (Tmx, −d 2) before 5-FU injection (d 0). Mice were collected at 2 (d 2), 4 (d 4), 7 (d 7), and 14 (d 14) d after 5-FU injection. Troy^{GFP}+ NSCs and DCX+KI67− NBs survive the treatment. (*B*) Quantification of the clonal analysis at d 7 and d 14. S, size; T, total percentage for each row or column. (*C*) Examples of Troy^{GFP}+ activated NSCs at d7. At this stage, clones are exclusively formed of Troy^{GFP}+ NSCs. (*D*) Examples of activated (*Left*) as well as quiescent (*Right*) NSCs within clones at d 14. (*E*) Clonal distribution of Troy^{GFP}+ NSCs 14 d after Tmx induction is similar between unperturbed and injured (5-FU) conditions. (*F*) Treatment with 5-FU in Ki67$^{iresCreER\ +/HET}$ Rosa$^{tdTomato\ +/HET}$ mice. (*Left*) Treatment with 5-FU (d 0) 1 d before Tmx induction (d 1) kills the majority of recombined cells (analyzed at d 2). (*Right*) When 5-FU is treated 1 d after Tmx induction, some of the tdTomato+DCX+ NBs and tdTomato+KI67− cells contacting the ventricles survive. (*G*) Quantification of *F*. [Scale bars: *A*, 50 μm; *C* and *D*, 20 μm (*Upper Images*) and 10 μm (*Lower Images*); *F*, 50 μm (*Upper*) and 20 μm (*Lower*)].

a major loss of recombined cells (3.3 ± 4.0 tdTomato+ cells per mm^2) compared with controls (835.9 ± 124.9 tdTomato+ cells per mm^2; Fig. 6 *F* and *G*); 92 ± 10% of the remaining rare tdTomato+ cells were KI67+ (Fig. 6*F*). These findings confirm that the Ki67^{iresCreER} allele is specifically active in proliferating cells. When Tmx was administered 1 d before (−d 1) 5-FU treatment (d 0), some of the tdTomato+ cells survived, indicating that they exit the cell cycle before 5-FU treatment is effective (27% of controls, Fig. 6 *F* and *G*); 89 ± 5% of the remaining tdTomato+ cells were DCX+ NBs that left the cell cycle (Fig. 6 *F* and *G*), while the remaining (11 ± 5%) KI67−DCX− cells were seen on the surface of the SEZ at d2 (Fig. 6*F*); 11 ± 0% of tdTomato+ clones contained multiple cells, consistent with aNSCs' being able to increase their number and return to quiescence within 1 d (Fig. 6*G* and *SI Theory*).

In summary, these results suggest that, following injury, the depletion of aNSCs is compensated by the rapid activation of qNSCs that quickly expand to repopulate the closed niche and reestablish neurogenesis. However, during this process, until day 14 after injury the proliferative activity of aNSCs is sustained at a higher rate than under homeostatic conditions.

Discussion

Despite extensive investigation, the molecular identity and long-term fate behavior of individual adult NSCs of the SEZ have remained in question. By combining long-term lineage tracing assays using two knock-in alleles (not previously explored in the brain) with quantitative clonal analysis we have proposed a model in which NSCs may transit reversibly between the quiescent and active compartments. When active, the fate of NSCs is chosen stochastically, with probabilities correlated with the number of neighboring NSCs in their localized niche. As a result, NSCs are rarely lost altogether from within a niche, while their capacity to expand becomes increasingly suppressed as their number grows locally. Consistent with the arrangement of NSCs and astrocytes in pinwheel structures, our results support the presence of multiple physically separated niche structures within the SEZ.

We provide a comprehensive, high-quality transcriptome atlas of the adult neurogenic niche with single cells from 11 FACS-purified populations. Direct comparison of Troy^{GFP} and Slc1a3+ EGFR− cells reveal a large overlap between both populations, suggesting that Troy is expressed by a large population of qNSCs. Our clustering algorithm did not detect any Slc1a3-high astrocytes reported by Llorens-Bobadilla et al. (15), which we attribute to either technical problems in detecting astrocytes or to differences in the region cells were isolated (*SI Theory*). Important to this study, we identify a large aNSC pool with diverse gene expression pattern.

In the course of NSC division, key transcriptional factors compete to regulate NSC self-renewal and differentiation. With emphasis placed on division asymmetry of NSCs, it has been assumed that commitment to differentiation occurs at, or immediately after, stem cell division, triggering a strictly unidirectional differentiation pathway (61). By contrast, our findings indicate that stem-cell maintenance is achieved through a process of niche-based population asymmetry. The decision to differentiate or reenter quiescence takes place after an initial expansion of NSCs within their niche. In particular, tracings based on both Troy^{GFPiresCreER} and Ki67^{iresCreER} revealed that multiple qNSCs might be generated by a single aNSC. Consistently, injury-activated NSCs expand their number before returning to quiescence. Moreover, single-cell RNA sequencing shows that proliferating Troy+ NSCs display a complex and diverse gene expression pattern. Gene modules, composed of genes with highly correlated expression patterns, are activated separately and in a partially overlapping manner in aNSCs. Some of the genes are shared with Troy− TA cells and NBs, suggesting that a differentiation program is activated in aNSCs. This likely results in decreased probability of return to quiescence. This continuum from quiescence to differentiation fits well with our clonal tracing data; following NSC activation, the composition of

clones is not fixed but depends on the stochastic fate decisions of aNSCs to proliferate or differentiate. These findings strongly suggest that stem-cell potential is distributed between active and qNSC populations.

The self-renewal potential of NSCs in the adult hippocampus remains controversial. While Encinas et al. (32) suggest that aNSCs eventually differentiate into mature astrocytes, Bonaguidi et al. (62) provide evidence based on clonal lineage tracing that individual NSCs may be long-term self-renewing. In support, Urbán et al. (28) suggest that long-term self-renewal of NSCs is achieved through return to a transient quiescent state. Similarly, the ability of dividing SEZ stem cells to return to long-term quiescence has been debated. A recent study employing clonal lineage tracing from Slc1a3+ NSCs suggested their depletion following limited rounds of division as a manifestation of aging (33). Similarly, lineage tracing of embryonic precursors of adult NSCs suggests that individual NSCs might only be active for limited periods throughout adulthood (34). In contrast, our results, based on the Ki67^{iresCreER} allele, provide clear evidence that some aNSCs return to quiescence. Combined with our clonal tracing data, we found that NSCs are then activated again after a refractory period of ∼3 wk on average, during which time the TA population becomes exhausted. Thus, neuronal production is not continuous at the level of individual progenitors, but follows a pattern of "boom-and-bust" (Fig. 7). Cells that have proliferated in young adults remain potent even after a year; they can reenter the cell cycle and generate new neurons. Whether these Troy+ qNSCs display sporadic activation or remain dormant during this period remains to be seen. However, we observe that a large fraction of NSCs are quiescent at d 60, suggesting that there might be long periods of inactivity following repeated cycles of activation. Our quantitative analysis does not provide evidence for functionally distinct qNSCs. However, activation of a large pool of qNSCs upon injury as well as our single-cell analysis suggest that both dormant and sporadically activated qNSCs may coexist. As we used different induction protocols compared with previous studies, the apparent discrepancy may arise from labeling functionally different stem-cell states. Indeed, if Slc1a3+ NSCs were more likely labeled in an active state or in niches containing multiple NSCs, our model would predict that they are more likely to be "displaced" by neighboring stem cells, resulting in commitment to differentiation.

Multiple studies indicate a loss of NSC number with age that can, at least in part, be restored by "youth-related" signals (63). To avoid conflating the question of the fate of NSC during homeostatic turnover with mechanisms of age-related NSC loss, mice induced at 8–10 wk of age were analyzed up to ∼10 mo of age when neurogenesis is at levels comparable to those in young adults (64).

The cellular and molecular mechanisms by which the niche controls NSC numbers have remained an intriguing open question. Our model suggests that the self-renewal capacity of NSCs decreases with the number of NSCs that occupy the same closed niche. In common with intestinal stem cells (65), the short-term self-renewal potential and molecular identity of NSCs in the adult SEZ is not invariant but changes in response to local extrinsic cues. Based on the current findings, a mechanism in which the fate behavior of Troy+ NSCs is correlated with the number of neighboring stem cells provides the most likely explanation of the clonal dynamics (Fig. 7). At the molecular level, such competition could be mediated through limited access to the ventricular and endothelial surfaces, a limited supply of niche factors produced by other SEZ cell types, or an inhibitory effect of direct cell-to-cell contact of NSCs. The functional study of differentially regulated genes identified by single-cell transcriptome profiling in this study and others (15, 47, 66) could provide a starting point for addressing the molecular interactions that mediate the regulation of NSC number.

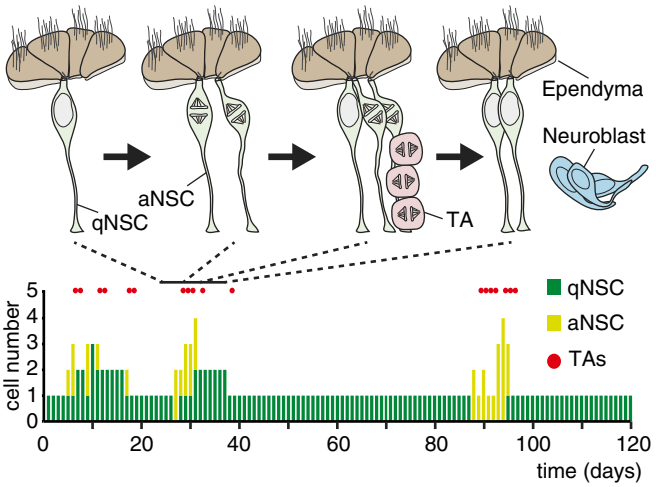

Fig. 7. A closed niche model of adult neurogenesis. Schematic representation of the NSC niche at selected time points. The lower plot depicts the result of a numerical simulation of the model dynamics with the inferred parameters showing changes in the number of quiescent and aNSCs as well as the production of TA cells at given time points. These simulations reveal a pattern of stochastic dynamics in which the sporadic entry of qNSCs into the cycle leads to a burst of proliferative activity leading to TA cell production before a return to quiescence.

Methods

A detailed description of materials and methods can be found in *SI Methods*.

Contact for Reagents and Resource Sharing. Requests for reagents should be directed to Hans Clevers at h.clevers@hubrecht.eu.

Mouse Strains Used in This Study. Troy^{GFPiresCreER} mice were described before (41). Ki67^{iresCreER} mice were generated by homologous recombination in embryonic stem cells targeting an iresCreERT2 cassette at the transcriptional stop site of *mKi67* (Fig. S6*A*). Details of embryonic stem cell targeting are described elsewhere (67). Rosa^{LacZ}, Rosa^{YFP}, and Rosa^{tdTomato} (Jackson Laboratory) mice were used for lineage tracing in Troy^{GFPiresCreER} (Rosa^{LacZ} and Rosa^{YFP}) and Ki67^{iresCreER} (Rosa^{tdTomato}) mice. All mice were bred on a C57BL/6 background. All animal procedures and experiments were performed in accordance with national animal welfare laws under a project license obtained from the Dutch government, and were reviewed by the Animal Ethics Committee of the Royal Netherlands Academy of Arts and Sciences. All rodents are housed in a barrier facility in conventional cages and are changed without using a change station. All personnel entering the barrier must wear protective clothing (including caps and special clogs). All animals are received directly from approved vendors (Charles River) or generated in-house. Animals arriving from other sources must pass the GDL quarantine for screening or by embryo transfer. After screening these specific-pathogen-free mice are housed in micro isolator cages and are transferred to the Hubrecht laboratory. Details of the lineage tracing experiments, 5-FU treatment and the number of mice are described in *SI Methods*.

Single-Cell RNA Sequencing. RNA samples were prepared using a modified version of the CEL-seq protocol as described previously, with a few modifications (49, 68). Data processing is described in *SI Methods* and *SI Theory*.

Statistical Analysis. Data are presented as mean ± SD. When two groups of samples were compared, *P* values were calculated using the unpaired, two-tailed Student's *t* test.

ACKNOWLEDGMENTS. We thank Anko de Graaff for imaging support, Maaike van den Born for excellent technical assistance with mouse experiments, Harry Beugthel for help with histology, Jeroen Korving for ES cell injections, Stefan van der Elst for assistance with FACS sorting, Prof. Okano for kindly providing reagents, all members of the H.C. and B.D.S. group for useful discussions, and the Hubrecht Institute animal caretakers for animal support. This work was supported by NIRM/ Clevers and

Stichting Vrienden van het Hubrecht (O.B.), EU/232814-StemCellMark and Skolkovo 077 MPA (J.H.v.E.), NIH/MIT Subaward 5710002735 (to D.E.S.), KWF/PF-HUBR 2007-3956 and Stichting Vrienden van het Hubrecht (M.v.d.W.), European Research Council Advanced Grant ERC-AdG 294325-GeneNoiseControl (to K.W. and A.v.O.), and Wellcome Trust Grant 098357/Z/12/Z (to B.D.S.).

1. Li L, Clevers H (2010) Coexistence of quiescent and active adult stem cells in mammals. *Science* 327:542–545.
2. García-Verdugo JM, Doetsch F, Wichterle H, Lim DA, Alvarez-Buylla A (1998) Architecture and cell types of the adult subventricular zone: In search of the stem cells. *J Neurobiol* 36:234–248.
3. Doetsch F, Caillé I, Lim DA, García-Verdugo JM, Alvarez-Buylla A (1999) Subventricular zone astrocytes are neural stem cells in the adult mammalian brain. *Cell* 97:703–716.
4. Ahn S, Joyner AL (2005) In vivo analysis of quiescent adult neural stem cells responding to sonic hedgehog. *Nature* 437:894–897.
5. Shen Q, et al. (2008) Adult SVZ stem cells lie in a vascular niche: A quantitative analysis of niche cell-cell interactions. *Cell Stem Cell* 3:289–300.
6. Ernst A, et al. (2014) Neurogenesis in the striatum of the adult human brain. *Cell* 156: 1072–1083.
7. Spalding KL, et al. (2013) Dynamics of hippocampal neurogenesis in adult humans. *Cell* 153:1219–1227.
8. Lim DA, Alvarez-Buylla A (2014) Adult neural stem cells stake their ground. *Trends Neurosci* 37:563–571.
9. Mirzadeh Z, Merkle FT, Soriano-Navarro M, Garcia-Verdugo JM, Alvarez-Buylla A (2008) Neural stem cells confer unique pinwheel architecture to the ventricular surface in neurogenic regions of the adult brain. *Cell Stem Cell* 3:265–278.
10. Paez-Gonzalez P, et al. (2011) Ank3-dependent SVZ niche assembly is required for the continued production of new neurons. *Neuron* 71:61–75.
11. Tong CK, et al. (2014) Axonal control of the adult neural stem cell niche. *Cell Stem Cell* 14:500–511.
12. Silva-Vargas V, Maldonado-Soto AR, Mizrak D, Codega P, Doetsch F (2016) Age-dependent niche signals from the choroid plexus regulate adult neural stem cells. *Cell Stem Cell* 19:643–652.
13. Ihrie RA, et al. (2011) Persistent sonic hedgehog signaling in adult brain determines neural stem cell positional identity. *Neuron* 71:250–262.
14. Kriegstein A, Alvarez-Buylla A (2009) The glial nature of embryonic and adult neural stem cells. *Annu Rev Neurosci* 32:149–184.
15. Llorens-Bobadilla E, et al. (2015) Single-cell transcriptomics reveals a population of dormant neural stem cells that become activated upon brain injury. *Cell Stem Cell* 17: 329–340.
16. Givogri MI, et al. (2006) Notch signaling in astrocytes and neuroblasts of the adult subventricular zone in health and after cortical injury. *Dev Neurosci* 28:81–91.
17. Nyfeler Y, et al. (2005) Jagged1 signals in the postnatal subventricular zone are required for neural stem cell self-renewal. *EMBO J* 24:3504–3515.
18. Androutsellis-Theotokis A, et al. (2006) Notch signalling regulates stem cell numbers in vitro and in vivo. *Nature* 442:823–826.
19. Basak O, Giachino C, Fiorini E, Macdonald HR, Taylor V (2012) Neurogenic subventricular zone stem/progenitor cells are Notch1-dependent in their active but not quiescent state. *J Neurosci* 32:5654–5666.
20. Veeraraghavalu K, Choi SH, Zhang X, Sisodia SS (2010) Presenilin 1 mutants impair the self-renewal and differentiation of adult murine subventricular zone-neuronal progenitors via cell-autonomous mechanisms involving notch signaling. *J Neurosci* 30: 6903–6915.
21. Ramírez-Castillejo C, et al. (2006) Pigment epithelium-derived factor is a niche signal for neural stem cell renewal. *Nat Neurosci* 9:331–339.
22. Colak D, et al. (2008) Adult neurogenesis requires Smad4-mediated bone morphogenic protein signaling in stem cells. *J Neurosci* 28:434–446.
23. Doetsch F, Petreanu L, Caille I, Garcia-Verdugo JM, Alvarez-Buylla A (2002) EGF converts transit-amplifying neurogenic precursors in the adult brain into multipotent stem cells. *Neuron* 36:1021–1034.
24. Calvo CF, et al. (2011) Vascular endothelial growth factor receptor 3 directly regulates murine neurogenesis. *Genes Dev* 25:831–844.
25. Lehtinen MK, et al. (2011) The cerebrospinal fluid provides a proliferative niche for neural progenitor cells. *Neuron* 69:893–905.
26. Ottone C, et al. (2014) Direct cell-cell contact with the vascular niche maintains quiescent neural stem cells. *Nat Cell Biol* 16:1045–1056.
27. Kokovay E, et al. (2010) Adult SVZ lineage cells home to and leave the vascular niche via differential responses to SDF1/CXCR4 signaling. *Cell Stem Cell* 7:163–173.
28. Urbán N, et al. (2016) Return to quiescence of mouse neural stem cells by degradation of a proactivation protein. *Science* 353:292–295.
29. Göritz C, Frisén J (2012) Neural stem cells and neurogenesis in the adult. *Cell Stem Cell* 10:657–659.
30. Gómez-López S, Lerner RG, Petritsch C (2014) Asymmetric cell division of stem and progenitor cells during homeostasis and cancer. *Cell Mol Life Sci* 71:575–597.
31. Bond AM, Ming GL, Song H (2015) Adult mammalian neural stem cells and neurogenesis: Five decades later. *Cell Stem Cell* 17:385–395.
32. Encinas JM, et al. (2011) Division-coupled astrocytic differentiation and age-related depletion of neural stem cells in the adult hippocampus. *Cell Stem Cell* 8:566–579.
33. Calzolari F, et al. (2015) Fast clonal expansion and limited neural stem cell self-renewal in the adult subependymal zone. *Nat Neurosci* 18:490–492.
34. Fuentealba LC, et al. (2015) Embryonic origin of postnatal neural stem cells. *Cell* 161: 1644–1655.
35. Barbosa JS, et al. (2015) Neurodevelopment. Live imaging of adult neural stem cell behavior in the intact and injured zebrafish brain. *Science* 348:789–793.
36. Paridaen JT, Huttner WB (2014) Neurogenesis during development of the vertebrate central nervous system. *EMBO Rep* 15:351–364.
37. Clevers H, Loh KM, Nusse R (2014) Stem cell signaling. An integral program for tissue renewal and regeneration: Wnt signaling and stem cell control. *Science* 346:1248012.
38. Azim K, et al. (2014) Persistent Wnt/β-catenin signaling determines dorsalization of the postnatal subventricular zone and neural stem cell specification into oligodendrocytes and glutamatergic neurons. *Stem Cells* 32:1301–1312.
39. Zhu Y, et al. (2014) Phosphatase WIP1 regulates adult neurogenesis and WNT signaling during aging. *J Clin Invest* 124:3263–3273.
40. Ortega F, et al. (2013) Oligodendrogliogenic and neurogenic adult subependymal zone neural stem cells constitute distinct lineages and exhibit differential responsiveness to Wnt signalling. *Nat Cell Biol* 15:602–613.
41. Stange DE, et al. (2013) Differentiated Troy+ chief cells act as reserve stem cells to generate all lineages of the stomach epithelium. *Cell* 155:357–368.
42. Fafilek B, et al. (2013) Troy, a tumor necrosis factor receptor family member, interacts with lgr5 to inhibit wnt signaling in intestinal stem cells. *Gastroenterology* 144: 381–391.
43. Hisaoka T, Morikawa Y, Senba E (2006) Characterization of TROY/TNFRSF19/TAJ-expressing cells in the adult mouse forebrain. *Brain Res* 1110:81–94.
44. Pastrana E, Cheng LC, Doetsch F (2009) Simultaneous prospective purification of adult subventricular zone neural stem cells and their progeny. *Proc Natl Acad Sci USA* 106: 6387–6392.
45. Hashimshony T, et al. (2016) CEL-Seq2: Sensitive highly-multiplexed single-cell RNA-seq. *Genome Biol* 17:77.
46. Muraro MJ, et al. (2016) A single-cell transcriptome atlas of the human pancreas. *Cell Syst* 3:385–394.e3.
47. Dulken BW, Leeman DS, Boutet SC, Hebestreit K, Brunet A (2017) Single-cell transcriptomic analysis defines heterogeneity and transcriptional dynamics in the adult neural stem cell lineage. *Cell Rep* 18:777–790.
48. Basak O, et al. (2014) Mapping early fate determination in Lgr5+ crypt stem cells using a novel Ki67-RFP allele. *EMBO J* 33:2057–2068.
49. Grün D, et al. (2015) Single-cell messenger RNA sequencing reveals rare intestinal cell types. *Nature* 525:251–255.
50. Giachino C, et al. (2014) Molecular diversity subdivides the adult forebrain neural stem cell population. *Stem Cells* 32:70–84.
51. Liu HK, et al. (2008) The nuclear receptor tailless is required for neurogenesis in the adult subventricular zone. *Genes Dev* 22:2473–2478.
52. Kim EJ, Ables JL, Dickel LK, Eisch AJ, Johnson JE (2011) Ascl1 (Mash1) defines cells with long-term neurogenic potential in subgranular and subventricular zones in adult mouse brain. *PLoS One* 6:e18472.
53. Ji Z, Ji H (2016) TSCAN: Pseudo-time reconstruction and evaluation in single-cell RNA-seq analysis. *Nucleic Acids Res* 44:e117.
54. Bodenhofer U, Kothmeier A, Hochreiter S (2011) APCluster: An R package for affinity propagation clustering. *Bioinformatics* 27:2463–2464.
55. Mirzadeh Z, Doetsch F, Sawamoto K, Wichterle H, Alvarez-Buylla A (2010) The subventricular zone en-face: Wholemount staining and ependymal flow. *J Vis Exp* 39: 1938.
56. Costa MR, et al. (2011) Continuous live imaging of adult neural stem cell division and lineage progression in vitro. *Development* 138:1057–1068.
57. Ponti G, et al. (2013) Cell cycle and lineage progression of neural progenitors in the ventricular-subventricular zones of adult mice. *Proc Natl Acad Sci USA* 110: E1045–E1054.
58. Simons BD, Clevers H (2011) Strategies for homeostatic stem cell self-renewal in adult tissues. *Cell* 145:851–862.
59. Hutchins JR, et al. (2010) Systematic analysis of human protein complexes identifies chromosome segregation proteins. *Science* 328:593–599.
60. Han R, et al. (2008) Systemic 5-fluorouracil treatment causes a syndrome of delayed myelin destruction in the central nervous system. *J Biol* 7:12.
61. Goodell MA, Nguyen H, Shroyer N (2015) Somatic stem cell heterogeneity: Diversity in the blood, skin and intestinal stem cell compartments. *Nat Rev Mol Cell Biol* 16:299–309.
62. Bonaguidi MA, et al. (2011) In vivo clonal analysis reveals self-renewing and multipotent adult neural stem cell characteristics. *Cell* 145:1142–1155.
63. Villeda SA, et al. (2011) The ageing systemic milieu negatively regulates neurogenesis and cognitive function. *Nature* 477:90–94.
64. Shook BA, Manz DH, Peters JJ, Kang S, Conover JC (2012) Spatiotemporal changes to the subventricular zone stem cell pool through aging. *J Neurosci* 32:6947–6956.
65. Ritsma L, et al. (2014) Intestinal crypt homeostasis revealed at single-stem-cell level by in vivo live imaging. *Nature* 507:362–365.
66. Luo Y, et al. (2015) Single-cell transcriptome analyses reveal signals to activate dormant neural stem cells. *Cell* 161:1175–1186.
67. Barker N, et al. (2007) Identification of stem cells in small intestine and colon by marker gene Lgr5. *Nature* 449:1003–1007.
68. Hashimshony T, Wagner F, Sher N, Yanai I (2012) CEL-Seq: Single-cell RNA-Seq by multiplexed linear amplification. *Cell Rep* 2:666–673.